

D-Band 2D MIMO FMCW Radar System Design for Indoor Wireless Sensing

Subbarao Korlapati and Reza Nikandish, *Senior Member, IEEE*

Abstract—In this article, we present an algorithm-hardware system design approach for the D-band 2D multi-input multi-output (MIMO) frequency-modulated continuous-wave (FMCW) radar in indoor wireless sensing. We propose a scaling approach for the SNR of the receiver (RX) and the output power of the transmitter (TX) with distance, which can significantly reduce power consumption of the radar array. 2D direction-of-arrival (DOA) estimation using the radar array in the presence of Gaussian noise is evaluated using the multiple signal classification (MUSIC) and the minimum-variance distortionless response (MVDR) algorithms, over 1–10 m indoor distance and 0–30 dB SNR of the RX. The MUSIC algorithm can provide higher accuracy and faster simulation for large arrays, for example more than 16 elements, while the MVDR algorithm outperforms for small arrays. Furthermore, we develop a hardware model for the 2D radar array to evaluate the power consumption of the TX, RX, and local oscillator (LO) distribution network. It is shown that the power consumption of the LO distribution network, which can dominate the power consumption of a large array operating in the D-band, can be reduced through a distribution strategy for the LO amplifiers within the LO network to compensate for passive losses. Performance of the D-band radar array is evaluated in the free-space and the through-wall indoor sensing scenarios. Specifically, a 64-element radar array using the MUSIC algorithm for 2D DOA estimation can achieve a root-mean-square error (RMSE) of $0.8^\circ/0.3^\circ$ at 10/20 dB SNR and 5 m distance. The required TX output power per radar element is estimated as $-26/-16$ dBm at 10/20 dB SNR in the free-space sensing. In the through-wall sensing, this increases to $-10/0$ dBm for clear glass, $3/13$ dBm for drywall, and excessively high levels of $24/34$ dBm for wood door, at 140 GHz.

Index Terms—D-band, direction of arrival (DOA), internet of things (IoT), millimeter-wave, multi-input multi-output (MIMO), radar, receiver (RX), sixth generation (6G), transmitter (TX), wireless sensing.

Millimeter-Wave frequency bands above 100 GHz are promising for the next generation of wireless communication, sensing, and imaging systems. The extremely wide bandwidths available in these bands can enable data rates on the order of 100 Gbps for communication and millimeter-scale resolutions for sensing and imaging. The D-band, 110–170 GHz, is considered a potential candidate for sixth generation (6G) mobile communications and radar systems [1]–[3]. Wireless sensing with mm-wave radars is a key technology for emerging applications in integrated radar-communication systems, autonomous vehicles, gesture recognition for human-computer interaction, contactless health monitoring, and medical imaging.

Recently, several developments are presented towards the realization of wireless communications and sensing above

100 GHz. These developments, in the system and circuit levels, include experimental verification of the Friis free-space path loss (FSPL) model [2], characterization of the propagation channel [4], modeling and measurement of surface scattering [2], loss measurements of outdoor and indoor materials [2], [5], and implementation of integrated transceivers [3], [6]–[13]. Silicon processes are preferred to III-V processes in most applications, despite the superior output power, efficiency, and noise performance of these processes (for example, GaN) [14], to achieve higher integration levels. State-of-the-art D-band silicon-based on-chip radars include 145 GHz frequency-modulated continuous-wave (FMCW) radar [6], 140 GHz FMCW radar with 25 GHz bandwidth [7], dual-mode W-band and D-band radar [9], 150 GHz joint radar-communication transceiver with 30 GHz bandwidth [10], and 155 GHz FMCW orthogonal frequency-division multiplexing (OFDM) radar with the chirp duration of 1–100 μ s [11].

Multi-input multi-output (MIMO) radars can provide high angular resolutions, the spatial diversity, and improved effective SNR of the received signals [15]–[19]. The popular MIMO radar architecture based on 1D uniform linear array (ULA) can only detect azimuth angle which is insufficient for many emerging indoor wireless sensing applications. For example, in contactless heart monitoring, it is essential to focus the transmitted signal on the position of the human heart to receive accurate reflection signals. A 2D MIMO array should be used to detect azimuth and elevation angular information [17]–[20], and combined with the range information perceived using FMCW signals, to realize 3D sensing/imaging systems.

The design and implementation of efficient D-band MIMO radars can be very challenging as a result of the multidisciplinary nature of the problem and many practical issues involved. However, the available approaches focus mainly on one aspect of the system design [3], [21]–[24]. In the *signal processing domain*, many algorithms are developed to improve the resolution of directional-of-arrival (DOA) estimation, imaging, and perception. In the *hardware level*, there are several developments in antennas, RF circuits, transceivers, and digital signal processors, mainly focused to achieve higher performance, while the improvements and issues related to the signal processing which can have important effects on the hardware requirements are overlooked.

In this paper, we develop an *algorithm-hardware system design* approach for the D-band 2D MIMO FMCW radar in indoor wireless sensing. Main contributions of this work can be summarized as follows.

- 1) We develop an *algorithm-hardware model* to connect the accuracy of DOA estimation algorithms with the features

of radar array hardware. The developed model is used to evaluate the performance of the radar array over 1–10 m distance in the free-space and through-wall indoor wireless sensing scenarios.

- 2) The direction finding accuracy of the 2D radar array is evaluated using two popular DOA estimation algorithms, multiple signal classification (MUSIC) [25] and minimum variance distortionless response (MVDR) [26], and it is shown that each of these algorithms can provide a superior accuracy and simulation speed under certain conditions.
- 3) We propose a *scaling approach* for the SNR of the radar receiver (RX) and the output power of the radar transmitter (TX) with distance. It is shown that this can significantly reduce the required TX output power and the power consumption of the radar array.
- 4) We develop a system-level model to evaluate the power consumption of the TX, RX, and LO distribution network of the radar array. The LO distribution network is shown to have a major contribution to the power consumption of the radar array, and a strategy is proposed to distribute the LO amplifiers across the network to compensate for losses with low power consumption overhead.

The paper is structured as follows. In Section I, the 2D MIMO FMCW radar model is presented. In Section II, the scaling approach for the SNR and output power is provided and the results of the 2D DOA estimation simulations are discussed. In Section III, a hardware model for the 2D radar array is developed to estimate the power consumption. In section IV, performance of the radar array is evaluated in the free-space and through-wall indoor wireless sensing scenarios. The investigation results and practical considerations are discussed in Section V. The conclusions are presented in Section VI.

I. 2D MIMO FMCW RADAR

A. MIMO Radar Architecture

We consider a uniform array of $N_x \times N_y$ radar elements, as shown in Fig. 1. This array can be constructed as a virtual array comprising N_{TX} transmitters (TX) and N_{RX} receivers (RX). The number of virtual array elements is given by $N_x N_y = N_{TX} N_{RX}$. The distances are selected such that the inter-element spacing is $\lambda/2$. In the D-band, $\lambda/2 \approx 1$ mm, which allows large arrays to be integrated on a small physical area, for example, a 100-element array on the $1 \text{ cm} \times 1 \text{ cm}$ area. This allows the radar array to be integrated into electronic devices (such as a modem) and provide wireless sensing capabilities.

B. MIMO Waveforms

In the MIMO radar, orthogonal waveforms are transmitted to simplify the separation of received signals [27]. This can be achieved by applying a multiplexing scheme to modulate the chirp sequence signal $S_{TX}(t)$ into the TX signals, $S_{TX,k}(t)$ for $k = 1, \dots, N_{TX}$, as shown in Fig. 2.

Time-division multiplexing (TDM) is the simplest MIMO radar architecture, in which only one TX transmits at a time

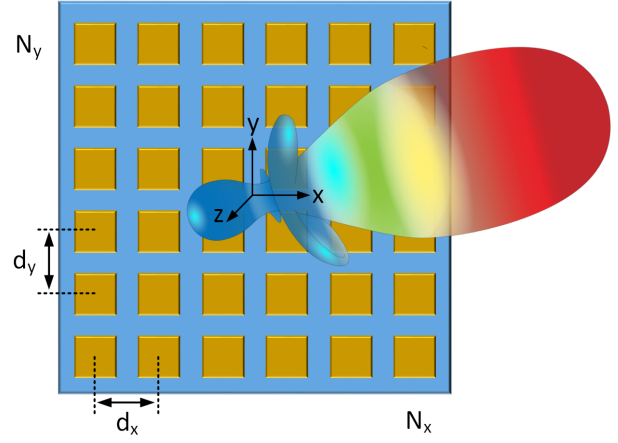


Fig. 1. Architecture of 2D MIMO radar comprising $N_x \times N_y$ virtual arrays. For a uniform array operating in the D-band, $d_x = d_y = \lambda/2 \approx 1$ mm.

slot, that is $x_k(t) = p[(t - \Delta t_k)/T]$, where $p(t)$ is the pulse function. However, this approach degrades the overall transmitted power, which is crucial for mm-wave bands. In the Doppler-division multiplexing (DDM) scheme, a phase code $x_k(t) = e^{j\Delta\Phi_k(t)}$ is applied with a specific pattern to realize different TX signals. In the orthogonal frequency-division multiplexing (OFDM) scheme, the TX signal is modulated by different carrier frequencies, which are usually shifted by an offset frequency $x_k(t) = e^{j[2\pi(k-1)\Delta f]t}$. In the DDM and OFDM MIMO architectures, all transmitters operate simultaneously and the total output power is enhanced. Therefore, we assume that the 2D MIMO array is realized using any of these multiplexing approaches, and any possible imperfections in the MIMO channels can be resolved through signal processing methods.

C. Range Resolution

The FMCW radar transmits a frame of multiple chirp signals, correlates the received target reflection with the transmit signal, and detects the target range using the signal time of flight. The transmit signal for each chirp can be modeled by a complex chirp signal defined as

$$S_{TX}(t) = A_{TX} e^{j(\omega_0 t + \pi S t^2)} \quad 0 \leq t \leq T_c, \quad (1)$$

where ω_0 is the chirp start frequency, $S = B/T_c$ is the chirp slope, B is the chirp bandwidth, and T_c is the chirp duration. This signal is repeated in time intervals $(k-1)T_c \leq t \leq kT_c$ for $k = 1, 2, \dots, N_c$, where N_c is the number of chirps in the frame (Fig. 2). The received signal can be derived as

$$S_{RX}(t) = A_{RX} e^{j[\omega_0(t-\tau) + \pi S(t-\tau)^2]}, \quad (2)$$

where $\tau = 2R/c$ is the radar signal time of flight and R is the target distance. The received signal is mixed with a scaled version of the transmit signal, and is passed through a bandpass filter (BPF) to achieve the IF signal as

$$S_{IF}(t) = A_{IF} e^{j(\omega_0 \tau - \pi \tau^2 S + 2\pi \tau S t)}. \quad (3)$$

This indicates a sinusoidal signal with the frequency of

$$f_{IF} = \tau S = \frac{2R}{c} \frac{B}{T_c}. \quad (4)$$

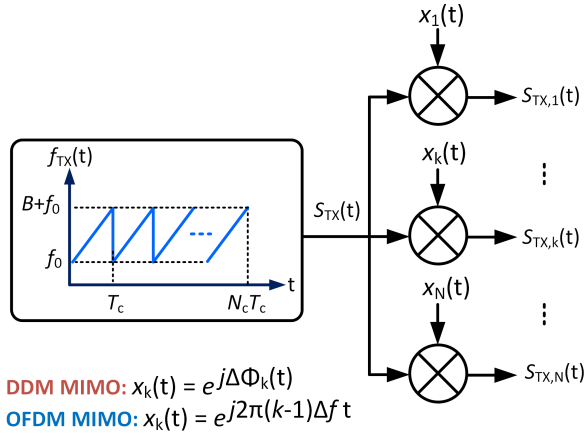


Fig. 2. Conceptual orthogonal waveform generation for MIMO FMCW radar. The chirp signal $S_{TX}(t)$ is modulated by the sequence $x_k(t)$ to realize the transmit signals $S_{TX,k}(t)$ for $k = 1, \dots, N_{TX}$.

TABLE I
STATE-OF-THE-ART D-BAND ON-CHIP FMCW RADARS.

Ref.	f_0 (GHz)	BW (GHz)	T_c (μ s)	P_{TX} (dBm)	N_{FRX} (dB)	Process
[6]	145	10	5-30	11.5*	8.0	28 nm CMOS
[7]	140	25	N/A	12.5	10.9	130 nm SiGe
[8]	122	20	N/A	13	N/A	130 nm SiGe
[9]	160	8	1000	13	N/A	130 nm SiGe
[10]	150	30	50	13	16	28 nm CMOS
[11]	155	8	1-100	9	7.5	22 nm FDSOI
[12]	122	10	1000	5	12.7	130 nm SiGe
[13]	145	18	80	9.4*	N/A	28 nm CMOS

* Effective Isotropic Radiated Power (EIRP)

The radar range resolution is derived as the minimum distance between two close targets that their corresponding IF frequencies fall into two consecutive range bins

$$\Delta R = \frac{c}{2B}. \quad (5)$$

Therefore, the wide bandwidth (60 GHz) available in the D-band can offer a fine range resolution (2.5 mm).

D. State-of-the-Art D-Band Radars

A performance summary of the state-of-the-art D-band on-chip FMCW radars is presented in Table I. A radar with 30 GHz bandwidth presented in [10] can provide a range resolution of 5.0 mm, which is promising for emerging sensing applications. Furthermore, ultrafast chirp signals, with a chirp sweep time of 1–100 μ s and the slope of 1–8 GHz/ μ s, can enable real-time high-resolution sensing scenarios. The TX output power is typically 10–13 dBm (10–20 mW) and the RX noise figure (NF) is 8–12 dB for the D-band on-chip radars. It should be noted that there is potential to further improve the radar performance in Table I. For example, the output power can be increased by combining output signals of multiple transistors.

E. Angular Resolution

The array factor for a 2D array can be derived as

$$AF(\theta, \phi) = \sum_{n=1}^{N_y} \sum_{m=1}^{N_x} e^{j[(m-1)\psi_x + (n-1)\psi_y]} \quad (6)$$

$$\psi_x = \beta d_x \sin \theta \cos \phi \quad (7)$$

$$\psi_y = \beta d_y \sin \theta \sin \phi \quad (8)$$

where $\beta = 2\pi/\lambda$ is the wave number, d_x and d_y are the inter-element spacing in the x and y directions, and (θ, ϕ) are the elevation and azimuth angles [28]. For the uniform array, $d_x = d_y = \lambda/2$. In Fig. 3, the magnitude of the array factor versus the azimuth and elevation angles is shown for different array sizes. A larger array provides higher directivity, narrower beamwidth, and lower side lobe level.

The angular resolution of the radar array can be derived as the separation between two consecutive nulls in the array factor $AF(\theta, \phi)$ versus the azimuth or elevation angle. The antenna elements have a limited beamwidth, which can be modeled as $|\phi| < \phi_{max}$ and $|\theta| < \theta_{max}$. This leads to the angular resolutions in the azimuth and elevation as

$$\Delta\phi \approx \frac{2}{N_x \cos \phi_{max}} \quad (9)$$

$$\Delta\theta \approx \frac{2}{N_y \cos \theta_{max}}. \quad (10)$$

Therefore, the number of array elements should be selected based on the required angular resolutions and the beamwidth of the antennas. For example, assuming a beamwidth of 45° in both azimuth and elevation, the number of array elements to achieve an angular resolution of 5° should be 25 × 25.

In the presence of noise and interference signals, certain signal processing algorithms should be used to extract the signal features and estimate the DOA of the targets. The accuracy is dependent on the radar array size and structure, the SNR level, and the algorithm. Effective SNR of the MIMO radar under optimal signal combining is improved by a factor equal to the number of virtual array elements compared to SNR of each radar element

$$SNR_{MIMO} = SNR_{SISO} + 10 \log_{10}(N_{TX} N_{RX}). \quad (11)$$

For example, by doubling the number of TX or RX elements, the SNR of the MIMO radar can be improved by 3 dB.

II. DOA ESTIMATION USING 2D RADAR ARRAY

A. MUSIC and MVDR Algorithms

It is assumed that the received signal vector $\mathbf{x}(t)$ comprises K source signals $\mathbf{s}(t)$ with unknown directions and additive white Gaussian noise (AWGN) $\mathbf{n}(t)$. The received signal vector is related to the source signal vector as

$$\mathbf{x}(t) = \mathbf{A}\mathbf{s}(t) + \mathbf{n}(t). \quad (12)$$

The array matrix \mathbf{A} is defined as

$$\mathbf{A} = [\mathbf{a}(\theta_1, \phi_1), \dots, \mathbf{a}(\theta_K, \phi_K)], \quad (13)$$

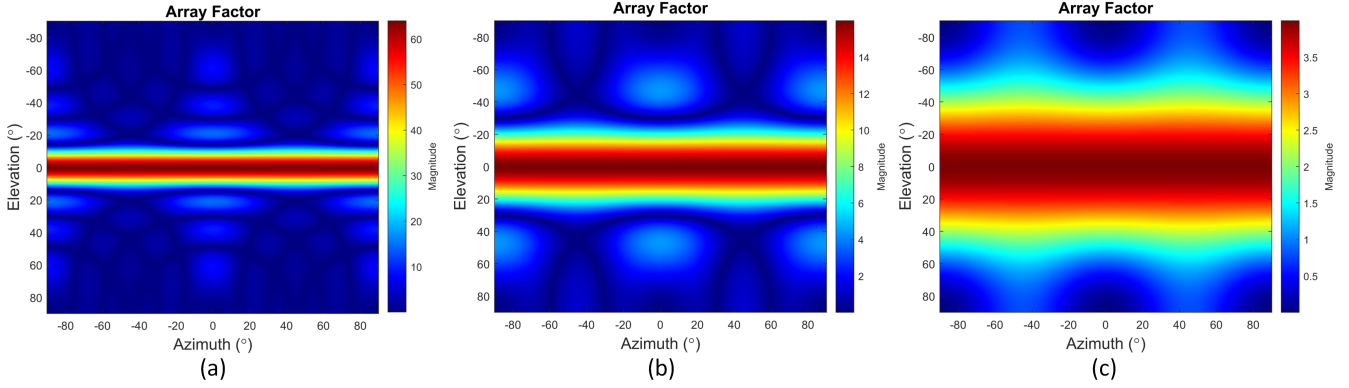


Fig. 3. Magnitude of the array factor for different structures: (a) 8×8 array, (b) 4×4 array, (c) 2×2 array.

where $\mathbf{a}(\theta, \phi) = [a_{mn}(\theta, \phi)]^T$, $a_{mn}(\theta, \phi)$ is the element of array factor in (6), (θ_k, ϕ_k) denotes angular coordinates of the k -th target, and K is the number of targets. The covariance matrix of the received signal is estimated using its time-domain samples (snapshots)

$$\hat{\mathbf{R}}_{xx} = \frac{1}{N_s} \sum_{k=1}^{N_s} \mathbf{x}[k] \mathbf{x}^H[k]. \quad (14)$$

The covariance matrix and the array matrix are used to construct a spatial spectrum function $P(\theta, \phi)$. In the MUSIC algorithm, $P(\theta, \phi)$ is related to the signal and noise subspace of the covariance matrix [25], while in the MVDR algorithm it is derived from the inverse of the covariance matrix [26]. Finally, a search algorithm is used to find peaks of the spatial spectrum function as DOA of the source signals.

B. Scaling of SNR and Output Power with Distance

In free space, the SNR of the received signal is derived as

$$\text{SNR} = \frac{P_{TX} G_{TX} G_{RX} \lambda^2 \sigma T_{meas}}{(4\pi)^3 k T F d^4}, \quad (15)$$

where P_{TX} is the TX output power, G_{TX} and G_{RX} are gain of the TX and RX antennas, λ is the signal wavelength, σ is the radar cross section (RCS) of the target, T_{meas} is the radar measurement time, $k = 1.38 \times 10^{-23}$ J/K, T is the absolute temperature, F is the RX noise factor, $\text{NF}_{RX} = 10 \log_{10}(F)$, and d is the target distance.

In classical DOA estimation problems, the SNR is considered as an independent parameter, and, as a result, it is independent of the target distance. However, this requires scaling of the TX output power with the distance as $P_{TX} \propto d^4$ [see (15)]. This can lead to an impractical TX output power requirement at long distances. On the other hand, if we assume a fixed TX output power, the RX SNR will decrease with the distance as $\text{SNR} \propto d^{-4}$. A compromise between the two extremes is to assume that both the TX output power and the RX SNR are scaled with the distance.

We propose a scaling approach for the RX SNR and TX output power with the distance as

$$\text{SNR}(d) = \text{SNR}(d_0) \left(\frac{d_0}{d} \right)^p \quad (16)$$

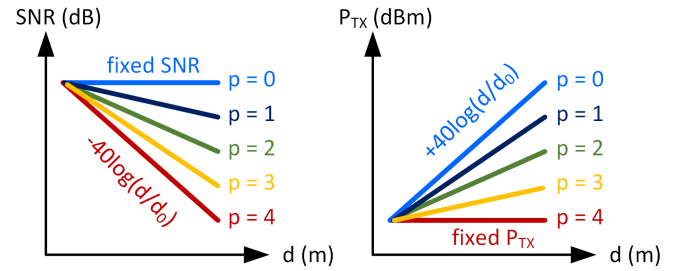


Fig. 4. Scaling of the RX SNR and the TX output power with distance. In the fixed SNR scenario (blue), the TX power should be increased with the slope of $+40 \log(d/d_0)$, while in the fixed TX power scenario (red), the SNR is reduced with the slope of $-40 \log(d/d_0)$. A compromise can be achieved by selecting a scaling exponent in the range $0 < p < 4$.

$$P_{TX}(d) = P_{TX}(d_0) \left(\frac{d_0}{d} \right)^{p-4}, \quad (17)$$

where p is the scaling exponent that should be selected in the range $0 \leq p \leq 4$ and d_0 is the reference distance. The TX output power is set to achieve a certain RX SNR at a reference distance d_0 , and it is scaled according to (17) at other distances. The classic constant SNR scenario is achieved for $p = 0$, while the case that the TX output power is constant corresponds to $p = 4$. Different conditions for the scaling of the SNR and TX output power with distance using (16) and (17) are presented in Fig. 4. We select $p = 2$ as a compromise between the slope of the SNR drop with distance and the increase in the required TX power.

C. DOA Estimation Results

The MUSIC and MVDR DOA estimation algorithms are evaluated for different 2D radar array architectures. The reference distance is assumed as $d_0 = 1$ m. Root-mean-square error (RMSE) is used as the accuracy metric to evaluate the algorithms

$$\text{RMSE} = \sqrt{\frac{1}{KM} \sum_{j=1}^M \sum_{i=1}^K \left((\hat{\phi}_i(j) - \phi_i)^2 + (\hat{\theta}_i(j) - \theta_i)^2 \right)}, \quad (18)$$

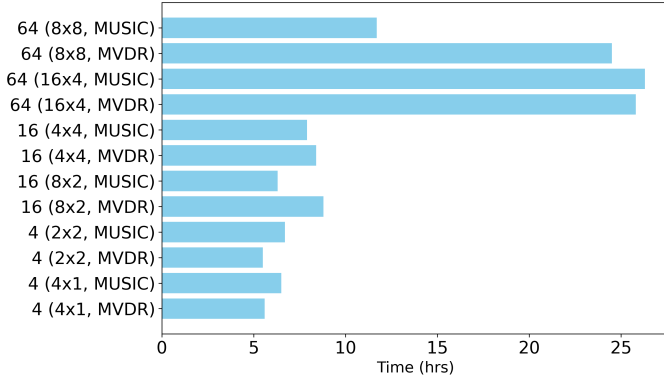


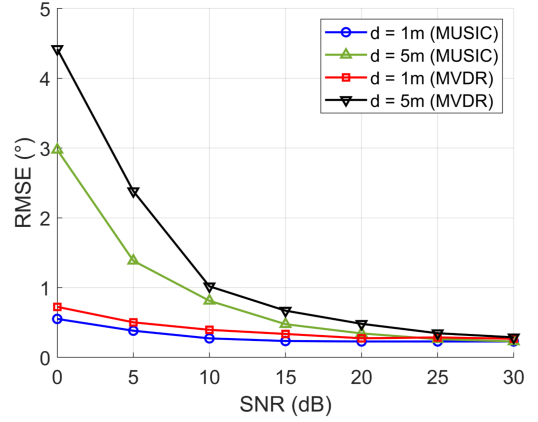
Fig. 5. Simulation times of the DOA estimation for different algorithms and array sizes.

where (ϕ_i, θ_i) is the actual DOA of the i -th target, $(\hat{\phi}_i(j), \hat{\theta}_i(j))$ is the estimated DOA of the i -th target in the j -th sample of the Monte Carlo runs, K is the number of targets, and M is the number of the Monte Carlo runs. We model the noise present in the received signal as a random Gaussian variable, $\sim \mathcal{N}(0, \sigma^2)$, with zero mean and a variance determined based on the SNR. We evaluated the simulation results for different numbers of runs and selected $M = 100$ to achieve high accuracy with practical simulation times. In this work, we assume that there are three targets, $K = 3$, with equal signal amplitudes.

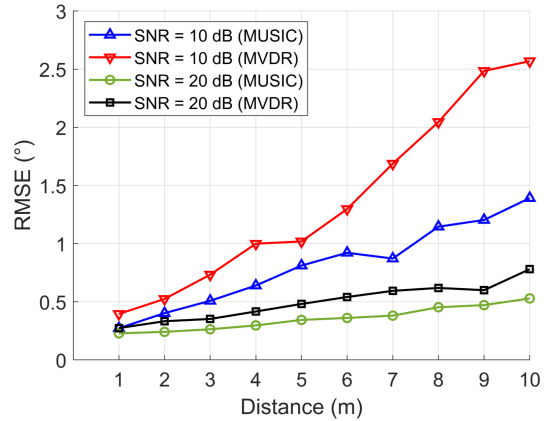
1) *64-Element Array*: For a 64-element array realized as an 8×8 square array, the RMSE in terms of SNR and distance is shown in Fig. 6. The SNR and the distance are, respectively, varied in the range of 0–30 dB and 1–10 m, as typical values in indoor wireless sensing scenarios. The MUSIC algorithm outperforms the MVDR algorithm in the all SNR levels and distances, especially at long-distance and low-SNR conditions. Fig. 6(a) indicates that at short distances, for example 1 m, the RMSE lower than 1° can be maintained even at very low SNR levels. This is the result of an improved SNR of the MIMO array that for the 64-element array is derived using (11) as $10 \log_{10}(64) \approx 18$ dB. As shown in Fig. 6(b), for the SNR of 20 dB, RMSE lower than 0.6° can be achieved across the 1–10 m distances using the MUSIC algorithm.

A 64-element array can be realized as other structures, for example, 16×4 , 32×2 , as a higher resolution in the azimuth angle compared to the elevation angle is usually required. Simulation results of these alternative array structures are not shown due to limited space. The DOA estimation results for the 16×4 array indicate RMSE of about $1.2 - 1.6^\circ$ for SNR of 0–30 dB at 1 m distance. Compared to the RMSE of the 8×8 array shown in Fig. 6(a), the RMSE of the 16×4 array is higher by 2x–3x. This can be due to reduced number of array elements in the vertical direction which leads to a lower elevation resolution.

Simulation times of the DOA estimation are shown in Fig. 5. Simulations are performed using an Intel Core i5-7300HQ 2.50 GHz CPU with 8 GB RAM. The simulation time comprises the time required to complete the simulations on an SNR of 0–30 dB with a step of 5 dB, a distance of 1–10 m with a step of 1 m, and 100 Monte Carlo runs. For the 8×8 array,



(a)



(b)

Fig. 6. RMSE for the MUSIC and MVDR algorithms with 8×8 radar array. MUSIC outperforms MVDR especially in the low-SNR conditions.

the MUSIC algorithm provides faster simulations and higher accuracy compared to the MVDR algorithm.

2) *16-Element Array*: For a 16-element array realized as a 4×4 structure, the RMSE in terms of the SNR and distance is shown in Fig. 7. Interestingly, the MUSIC and MVDR algorithms provide very close accuracy across the ranges of SNR and distance considered in the simulations. This is in contrary with the 8×8 array in which the MUSIC led to higher accuracy compared to the MVDR. The SNR improvement by the MIMO array is $10 \log_{10}(16) \approx 12$ dB. Fig. 7(b) indicates that with the 20 dB SNR, the RMSE lower than 2° can be achieved in the 1–10 m range. Moreover, Fig. 5 shows that the simulation times for the two algorithms are very close.

3) *4-Element Array*: A 4-element array can only provide a coarse DOA estimation, but its simpler hardware and lower power consumption can be very useful for new applications (for example, smart home appliances and health monitoring devices). The SNR boost by the MIMO structure is $10 \log_{10}(4) \approx 6$ dB for the 4-element array. The RMSE for a 2×2 array versus SNR and distance is shown in Fig. 8. In this case, the MVDR algorithm significantly outperforms the MUSIC algorithm. This is an important result indicating that the MVDR algorithm is more accurate for small radar arrays. Fig. 8(b) shows that with 20 dB SNR, RMSE lower than 6° can

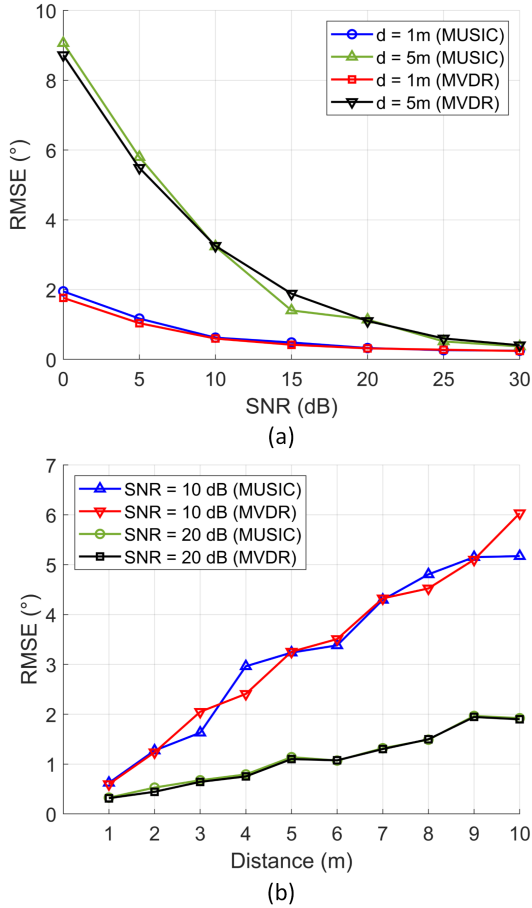


Fig. 7. RMSE for the MUSIC and MVDR algorithms with 4×4 radar array. MUSIC and MVDR provide very close results.

be achieved in 1–10 m using the MVDR algorithm. A higher SNR of 30 dB can reduce the RMSE to 0.4° at 1 m and 1.3° at 5 m [Fig. 8(a)]. Furthermore, Fig. 5 indicates that MVDR also features a simulation time 0.8x shorter than that of the MUSIC algorithm.

4) *Accuracy Versus the Number of Array Elements:* In Fig. 9, the RMSE is shown versus the number of array elements. The minimum RMSE achieved using the MUSIC and MVDR algorithms in each condition is presented here. This can be used to determine the number of elements of the array to achieve a desired RMSE for a specific SNR and distance.

III. HARDWARE OF 2D RADAR ARRAY

A. Array Architecture

A 2D radar array with $N_x \times N_y$ virtual elements can be realized through different numbers of TX and RX elements, and their physical arrangements. For a large radar array implemented on chip and operating in the D-band, the array architecture has significant effects on the performance, including the losses and power consumption of the LO distribution network and the TX-to-RX leakage signals.

We consider the architecture shown in Fig. 10, which comprises two linear arrays of RX and TX elements. This

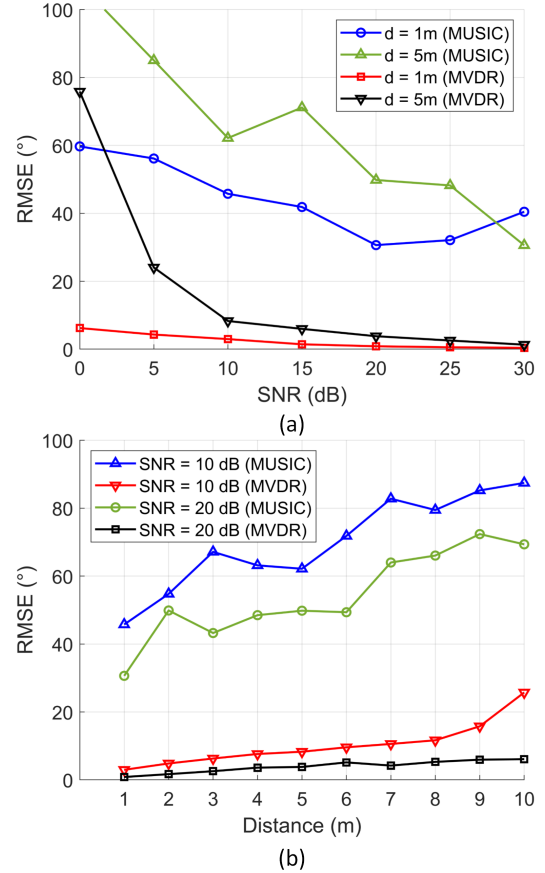


Fig. 8. RMSE for the MUSIC and MVDR algorithms with 2×2 radar array. MVDR outperforms MUSIC across all SNR and distance ranges.

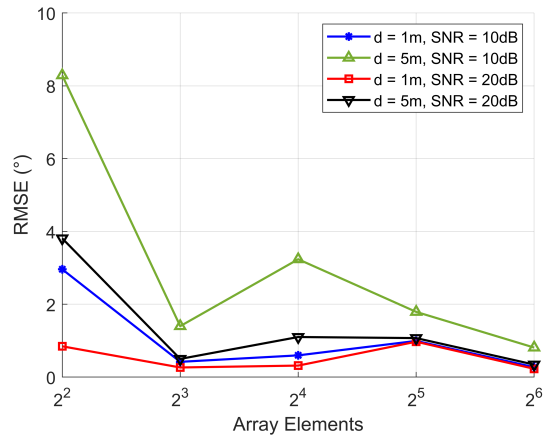


Fig. 9. RMSE versus the number of radar array elements. The minimum RMSE achieved using the MUSIC and MVDR algorithms is presented.

architecture allows for a symmetric LO distribution to the TX and RX elements. This leads to *correlated phase noise* in the TX and RX signals, which suppresses phase noise in the RX [6]. The D-band antenna array can be implemented using the antenna-in-package (AiP) technology and directly flip-chip attached to the chip die [29]. This allows the integration of large radar arrays with high radiation efficiencies (over 80%). We use this architecture to estimate the loss of the LO

distribution network, the required TX output power, and the power consumption of radar array.

B. LO Signal Distribution

Generation and distribution of the LO signal to the RX and TX elements is a major challenge in the large radar arrays operating in mm-wave bands. The LO generation comprises a phase-locked loop (PLL) and frequency multiplier(s) with low spurs, wide bandwidth, good chirp linearity, and high DC-to-RF efficiency. The LO distribution network comprises the routing paths to the TX and RX elements, and the LO amplifiers to compensate for the losses and maintain the signal integrity. The reference signal can be generated by an external PLL. We consider all of these circuit blocks as the LO distribution network, as shown in Fig. 10.

Frequency multipliers can be used at different locations in the radar array to upconvert the low-frequency reference signal to the D-band LO signals. Generally, some of the frequency multipliers can be shared between the TX and RX paths, and some others can be used separately in each TX and RX system. We can envision two extreme cases for the deployment of frequency multipliers. In the first approach, the reference signal is unconverted using a single high-performance frequency multiplier (usually comprising multiple stages) to the final RF signals and is then distributed between the TX and RX systems. The drawback is the greater loss of the LO distribution network and the higher power consumption of the LO amplifiers. In the second extreme approach, the low-frequency reference signal is distributed between the TX and RX paths, and is upconverted by dedicated frequency multipliers in the all TX and RX systems. This can reduce the losses of the LO distribution network and the power consumption of the LO amplifiers. However, this needs a total of $N_{TX} + N_{RX}$ frequency multipliers which can lead to high power consumption for large radar arrays. The optimal architecture should be between these two extremes, but it depends on many factors on the circuit and process level. In this work, we use the first approach to perform system simulations (see Fig. 10).

We assume that the output power of the reference chirp signal after being upconverted by the frequency multiplier is P_{REF} . The power of the reference signal is reduced by divisions in the paths and the passive losses, and reaches to $P_{LO,TX}$ in the TX and $P_{LO,RX}$ in the RX systems. Both of these LO power levels should be within certain ranges for their efficient operation. In the TX, the LO power should be high enough to push the PA into saturation and achieve high efficiency, as shown in Fig. 11(a). However, an excessively high LO power can degrade gain, power-added efficiency (PAE), defined as $PAE = (P_{out} - P_{in})/P_{DC}$, and the linearity of the PA. In the RX, the LO power should be high enough to enable switching of the differential pair transistors operating as the mixer, as shown in Fig. 11(b). On the other hand, for excessively large LO power levels, the conversion gain of the mixer, defined as $CG = P_{out,IF}/P_{in,RF}$, will degrade due to the operation of the transistor pair in the triode mode during most of the signal cycle [10]. Therefore, the LO power

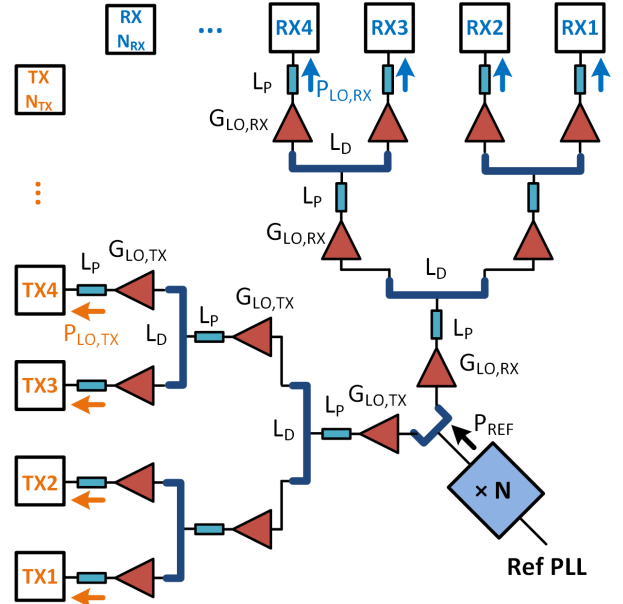


Fig. 10. Physical architecture of the 2D MIMO radar array realized using two linear arrays of TX and RX elements. LO signal distribution network includes loss of the LO signal paths L_P , loss of the power dividers L_D , the amplifiers with power gain of $G_{LO,TX}$ and $G_{LO,RX}$, used for loss compensation.

delivered to TX and RX should be maintained within optimal power ranges,

$$P_{LO,min} \leq P_{LO} \leq P_{LO,max}, \quad (19)$$

where the lower and upper limits of the LO power should be determined using properties of the circuit and fabrication process.

The reference signal is highly attenuated by the divisions between paths and the loss of on-chip transmissions lines in the D-band. Therefore, the LO amplifiers are distributed along the routing paths to prevent the need for a single high-gain LO amplifier after the reference signal generator. We propose to use *one LO amplifier in each path* with a power gain of $G_{LO,TX}$ in the TX paths and $G_{LO,RX}$ in the RX paths (see Fig. 10). The loss of the LO paths is dependent on their physical length, layout structure, and properties of the chip fabrication process. We assume that the length of all branches is Δl to simplify derivations. This length is dependent on the routing layout, but it can be fairly approximated by a fraction of the signal wavelength, for example, $\Delta l \approx \lambda/2$. The loss per unit length of the LO distribution paths can be estimated using the loss properties of transmission lines in the CMOS process (typically 1–3 dB/mm in the D-band). The loss of each path with the length of Δl is derived as L_P .

We can derive the LO power delivered to *each* of the TX and RX systems using Fig. 10 as

$$P_{LO,TX} = \frac{L_D (G_{LO,TX} L_P)^{\log_2 N_{TX}}}{N_{TX}} P_{REF} \quad (20)$$

$$P_{LO,RX} = \frac{L_D (G_{LO,RX} L_P)^{\log_2 N_{RX}}}{N_{RX}} P_{REF}, \quad (21)$$

where $G_{LO,TX}$ and $G_{LO,RX}$ are the gain of LO amplifiers in the TX and RX paths, L_D is the loss of the power dividers,

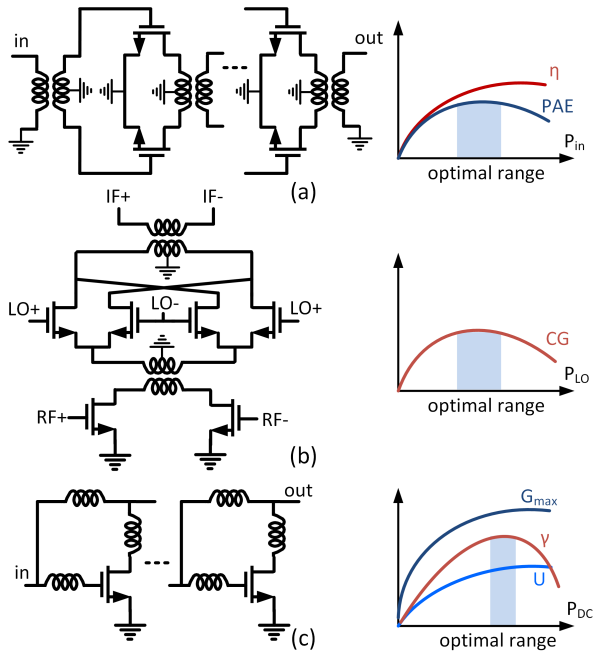


Fig. 11. Structure of typical mm-wave circuits used in the radar: (a) power amplifier circuit, and its efficiency η and PAE versus input power, (b) mixer circuit and its conversion gain (CG) versus LO power, (c) amplifier circuit with power gain boosting, and the maximum power gain G_{max} , unilateral power gain U , and the power gain efficiency $\gamma = G/P_{DC}$ of an amplifier stage versus power consumption.

and L_P is the loss of each LO path. These equations can be solved to derive the required gain of the LO amplifiers as

$$G_{LO,TX} = \frac{1}{L_P} \left(\frac{N_{TX} P_{LO,TX}}{L_D P_{REF}} \right)^{\frac{1}{\log_2 N_{TX}}} \quad (22)$$

$$G_{LO,RX} = \frac{1}{L_P} \left(\frac{N_{RX} P_{LO,RX}}{L_D P_{REF}} \right)^{\frac{1}{\log_2 N_{RX}}} \quad (23)$$

We can set the gain of LO amplifiers to completely compensate for the losses or even boost power of the reference signal if required. However, a higher gain of the LO amplifiers operating in the D-band can lead to significantly increased power consumption of the radar array. Therefore, gain of the LO amplifiers should be optimized based the required LO power and power consumption budget.

The total number of LO amplifiers in the TX path can be calculated using Fig. 10 as

$$N_{LO,TX} = 1 + 2 + \dots + \frac{1}{2} N_{TX} + N_{TX} = \sum_{k=0}^{\log_2 N_{TX}} 2^k, \quad (24)$$

which using $\sum_{k=0}^N r^k = (r^{N+1} - 1)/(r - 1)$ is derived as

$$N_{LO,TX} = 2N_{TX} - 1. \quad (25)$$

Similarly, for the RX path, the number of LO amplifiers can be derived as

$$N_{LO,RX} = 2N_{RX} - 1. \quad (26)$$

These results will be used to estimate power consumption of the LO distribution network in Section III-D.

C. TX Output Power

In the D-band, the efficiency of the silicon power amplifiers (PAs) is very low (typically 5–10%) [6], [8], [10], [11], [13], [30]. This can lead to huge power consumption for a large radar array. Therefore, it is essential to keep the required TX output power low using proper design strategies.

The required TX output power can be derived using (15), (16), and (17) as

$$P_{TX}(d) = \frac{(4\pi)^3 k T F d_0^p \text{SNR}(d_0)}{G_{TX} G_{RX} \lambda^2 \sigma T_{meas}} d^{4-p}. \quad (27)$$

This indicates that for $p < 4$, the required TX output power increases with the distance (see Fig. 4). Conventional DOA estimation approaches assume that the SNR is independent of the target distance, that is $p = 0$. However, (27) indicates that this requires the TX power to be increased proportional with d^4 . This can result in high power consumption in long indoor distances. In our proposed approach, we scale both the SNR and the TX output power with distance by selecting $p = 2$. This can significantly reduce the required TX output power and the power consumption of the radar array.

D. Power Consumption

In the silicon-based radar arrays operating beyond 100 GHz, the chip power density is significantly higher than that of the lower mm-wave bands, as a result of more compact chip size and reduced antenna spacing. The low power efficiency and gain of transistors, and the high loss of passive elements in the D-band further increase the power consumption of the radar array. Therefore, it is essential to develop a strategy to save the power consumption.

The power consumption of the radar array is dependent on the number of array elements, system architecture of the radar TX and RX, LO distribution network, circuit structures, and fabrication process. In the D-band, power consumption of the RX circuits is comparable with that of the TX circuits, and the LO distribution network can have a significant contribution which dominates the total power consumption. The power consumption can be estimated as

$$P_{DC} \approx P_{DC,TX} + P_{DC,RX} + P_{DC,LO}. \quad (28)$$

We derive each of the three terms versus the number of array elements and properties of the TX, RX, and the LO distribution circuits.

1) *TX Power Consumption*: In the TX system, the power consumption of each element is given by P_{TX}/η_{TX} , where η_{TX} is the TX efficiency. The power consumption of the all TX elements can be derived as

$$P_{DC,TX}(d) \approx \frac{N_{TX} P_{TX}(d)}{\eta_{TX}}. \quad (29)$$

In the radar array architecture considered in this work, the TX efficiency can be approximated by the PA efficiency, which is in the order of 5–10% for silicon-based PAs in the D-band [6], [8], [10], [11], [13], [30]. It is assumed that the TX circuits are reconfigured as the TX output power is scaled with the distance so that its efficiency remains almost the same. For the FMCW radars where a saturated PA can be

used, this is much less challenging than the communication systems using the amplitude-modulated signals. As a result, the power consumption of the TX system scales with the distance, proportional with the TX output power.

2) *RX Power Consumption:* The RX circuits with major power consumption include the low-noise amplifier (LNA), mixer, and baseband circuits (amplifiers and filters),

$$P_{DC,RX} \approx N_{RX}(P_{DC,LNA} + P_{DC,MIX} + P_{DC,BB}). \quad (30)$$

The power consumption of these circuits is dependent on many factors on the circuit and process level, and, as a result, cannot be accurately predicted before the circuits are designed. We can assume a fixed power consumption for each RX and scale it with the number of RX elements in the array. To find a practical estimate, we investigated the power consumption of the TX, RX, and LO parts in the D-band radars presented in the literature and noted that the power consumption of each RX element is usually on the order of 0.5x-1x the power consumption of each TX element [6], [9], [10], [12]. Therefore, we estimate the power consumption of an RX element using that of an TX element as $P_{DC,RX}/N_{RX} \approx \alpha P_{DC,TX}/N_{TX}$ with $\alpha \approx 0.75$. We should note that the RX power consumption is not scaled with the TX output power (unlike the TX). Therefore, $P_{DC,TX}$ should be evaluated using (29) at a fixed target distance, such as the reference distance d_0 .

3) *LO Power Consumption:* The LO distribution network comprises the LO amplifiers and frequency multiplier(s). The LO amplifiers are designed to achieve the maximum power gain, which is different with the design criteria of the PA. We define an efficiency metric namely the *power gain efficiency* for an LO amplifier as ratio of the power gain to the power consumption

$$\gamma = \frac{G}{P_{DC}}. \quad (31)$$

In mm-wave bands above 100 GHz, the gain of transistors is very low and usually an embedding passive network is used to boost it [31], [32]. The maximum power gain of transistor is given by

$$G_{\max} = (\sqrt{U} + \sqrt{U-1})^2, \quad (32)$$

where U is the unilateral power gain (Mason's invariant) that depends on the size and bias of the transistor and frequency [31]. By increasing the bias current, U initially increases but after a certain current level it is saturated. Therefore, we can assume that the transistor is biased at an optimum current with an associated unilateral power gain of U_{opt} . This also depends on the size of CMOS transistors. Using (31) and (32), we can conclude that this optimal current leads to the maximum γ [see Fig. 11(c)]. Usually, multiple amplifier stages should be cascaded to achieve the desired power gain.

The power consumption of the all LO amplifiers can be derived using (25), (26), and (31) as

$$P_{DC,LO} = \frac{(2N_{TX} - 1)G_{LO,TX}}{\gamma_{LO,TX}} + \frac{(2N_{RX} - 1)G_{LO,RX}}{\gamma_{LO,RX}}. \quad (33)$$

This equation along with (22) and (23) indicate that the power consumption of the LO network is dependent on the number of TX and RX elements, the power gain from the reference to

the LO signals, that is $P_{TX,LO}/P_{REF}$ and $P_{RX,LO}/P_{REF}$, the losses of the passive components, L_P and L_D , and the power gain efficiency of the transistors, $\gamma_{LO,TX}$ and $\gamma_{LO,RX}$.

We should also include the power consumption of the frequency multiplier(s), $P_{DC,M}$, in (33) for more accurate results. As we have considered the array architecture with a single frequency multiplier, its power consumption is not scaled with the number of TX and RX elements.

4) *Simulations:* The power consumption of the TX, RX, and LO distribution network versus the number of radar array elements $N_{TX}N_{RX}$ is shown in Fig. 12. The following assumptions are applied. The TX output power and efficiency are 10 dBm and 10%, the target distance is 1 m, and power consumption of the frequency multiplier is 50 mW. The LO distribution network provides 10 dB power gain from the reference signal to the LO signals, that is $P_{LO,TX}/P_{REF} = P_{LO,RX}/P_{REF} = 10$ in (22) and (23). The losses of the LO paths and the power dividers $L_P = 2$ dB and $L_D = 1$ dB. The power consumption of the LO distribution network is shown for two values of power gain efficiency. For example, $\gamma = 0.4$ (mW)⁻¹ means that the LO amplifiers offer power gain of 4 (6 dB) for 10 mW power consumption.

Fig. 12 indicates that the power consumption of the LO distribution network is dominant when the number of array elements is small. In this condition, each LO amplifier should provide a high gain to meet the required gain from the reference signal to the LO signals. This increases their power consumption. By increasing the number of array elements, two *competing effects* should be considered. First, the required gain of each LO amplifier is lower, as more LO amplifiers are cascaded and higher gain is achieved. This effect tends to reduce the power consumption of the LO amplifiers. Second, as the number of LO amplifiers increases with the number of array elements, (25) and (26), this effect tends to increase the power consumption. These two competing trends, can also be noted in (33), initially reduce the LO power consumption, leading to a flat area shown in Fig. 12, and then increase the LO power consumption as the second effect dominates.

The power consumption of the TX and RX systems increase proportional with the square root of the number of array elements (assuming $N_{TX} = N_{RX}$). For large number of array elements, the power consumption is dominated by the TX power consumption if the LO amplifiers feature a sufficient power gain efficiency. Otherwise, the power consumption of the LO distribution network will be dominant.

IV. INDOOR WIRELESS SENSING SCENARIOS

We consider the free-space and through-wall indoor wireless sensing scenarios. It is assumed that there is a dominant line-of-sight (LOS) wave propagation path between the radar array and the target, and the multipath effects are negligible. In the mm-wave bands above 100 GHz, the multipath signals are severely attenuated by multiple reflections from the indoor objects and walls, and their effect is less significant than in the lower frequency bands [2].

In the following simulations, the radar parameters are assumed as $G_{TX} = G_{RX} = 10$ dB, $\lambda = 2.1$ mm (at

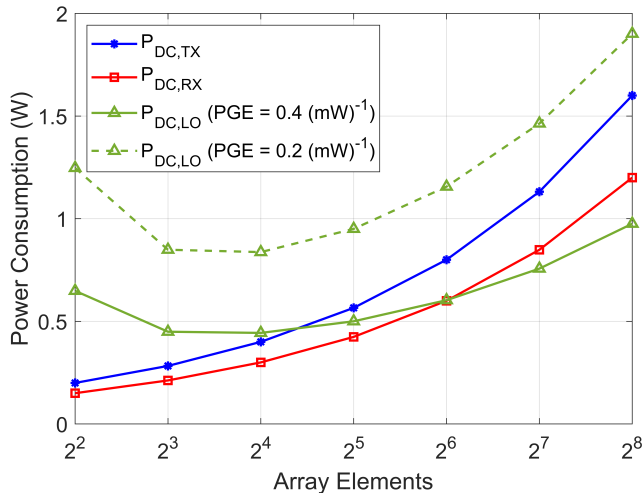


Fig. 12. Power consumption of the TX, RX, and LO distribution network versus the number of radar array elements. LO power consumption is shown for two values of power gain efficiency (PGE) γ .

140 GHz), $\sigma = 100 \text{ cm}^2$ as an estimate of the human hand RCS for gesture recognition applications [33], the chirp duration $T_c = 10 \mu\text{s}$, and $\text{NF}_{\text{RX}} = 10 \text{ dB}$ (Table I). The radar frame comprises 100 chirps and the measurement time is $T_{\text{meas}} = 100T_c = 1 \text{ ms}$.

A. Free-Space Sensing

In the free-space wireless sensing, the required TX output power versus the SNR and distance is shown in Fig. 13(a). The required TX output power can be read less than 0 dBm in most of the SNR and distance ranges. It reaches to a maximum of approximately 3 dBm at 30 dB SNR and 10 m distance. Comparing this with the TX output power of the state-of-the-art on-chip radars presented in Table I, indicates that the required TX output power in the free-space sensing is within the practical power levels of the available D-band radars. Furthermore, if we increase the SNR to 40 dB to improve the accuracy of the DOA estimation, or for a target with 10x smaller RCS, the required TX output power will increase to 13 dBm at the extreme distance of 10 m, which is still within the practical limits. It is important to note that these levels of required TX output power are achieved using our proposed scaling approach with distance. This investigation indicates the promise of high-resolution indoor wireless sensing in the free-space scenario.

B. Through-Wall Sensing

The through-wall wireless sensing has been successfully realized in the low RF bands (below 8 GHz) [34]. In these bands, the wireless signals can pass through the indoor walls with a moderate loss, but the signal wavelength is too large ($\lambda > 3 \text{ cm}$) and leads to coarse resolutions. The D-band can provide very fine resolutions ($\lambda \approx 2 \text{ mm}$), but its feasibility has not been explored in the literature yet. This inspires to use the developed model to investigate the required TX output power and the power consumption of the radar array for the through-wall wireless sensing in the D-band.

TABLE II
LOSS OF INDOOR MATERIALS MEASURED AT 140 GHz [2].

Material	Thickness	Loss
Clear Glass	0.6 cm	8.6 dB
Drywall	14.5 cm	15.0 dB
Wood Door	3.5 cm	25.5 dB

The loss of three representative indoor materials measured at 140 GHz [2] is presented in Table II. We assume that the penetration loss through the material is dominant and neglect other losses, including the surface scattering and multipath propagation. The loss of wall medium should be applied twice in the radar SNR to account for the transmitted signal from the radar and the reflected signal from the target

$$\text{SNR}_{\text{TW}} = \text{SNR} \times L_{\text{wall}}^2, \quad (34)$$

where L_{wall} is the loss of the wall material.

In Fig. 13(b), the required TX output power of each element versus the SNR and distance for sensing through clear glass is shown. The glass has 0.6 cm thickness and 8.6 dB measured loss at 140 GHz. The simulation conditions are the same as in the free-space case. A higher TX output power is required to compensate for the additional loss of the wall material. The required TX output power is within the practical limits for most of the SNR and distance ranges, except for extreme values at the top right of the figure. In Fig. 13(c), simulation results are presented for sensing through drywall with 14.5 cm thickness and 15.0 dB loss at 140 GHz. The required TX output power is higher than in the previous case due to the greater loss of drywall. In Fig. 13(d), simulation results are shown for sensing through wood door with 3.5 cm thickness and 25.5 dB loss at 140 GHz. The required TX output power is beyond the practical limits, except for in a small area around the bottom-left of the figure.

V. DISCUSSION

A comparison of the required TX output power versus the RX SNR for different indoor materials is shown in Fig. 14. The results are shown at two distances 1 m and 5 m. Fig. 14(a) indicates that the required TX output power at the distance of 1 m is very low in the all conditions. This is a promising result for the future of large radar arrays in short indoor distances. However, the required TX output power at 5 m distance can become very high and impractical in some conditions, as shown in Fig. 14(b).

The power consumption of the radar array with 64 elements versus the RX SNR is shown in Fig. 15. In the low SNR, the required TX power is low and the power consumption of the array is dominated by that of RX and LO, which are independent of the SNR. The required TX power becomes significant for the high SNR and large loss of indoor material, for example, the wood door in Fig. 15(a). This results in a power consumption sharply increasing with the SNR. The power consumption is higher for a longer target distance, as shown in Fig. 15(b).

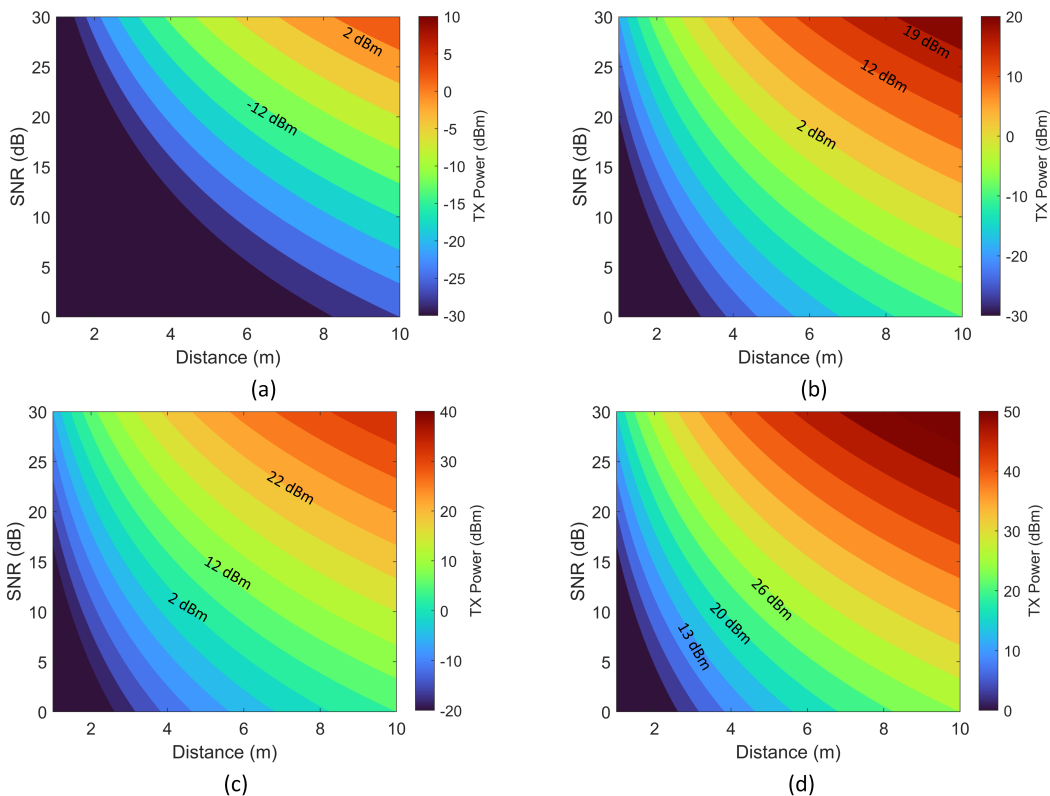


Fig. 13. Required output power per radar TX element versus SNR and distance in different wireless sensing scenarios: (a) free space, (b) clear glass, (c) drywall, (d) wood door. Loss of indoor materials in 140 GHz is extracted from the measurements (Table II) [2].

We evaluate the results of our investigations with practical considerations on the algorithm and hardware levels.

A. Number of Array Elements

The effective SNR of the MIMO radar can be improved by using more elements of the array to achieve a higher accuracy of DOA estimation. However, increasing the number of array elements can lead to several practical limitations, including higher power consumption, increased mutual coupling between antennas [24], self-interference, and spurs in the radar [23], greater loss in the LO signal distribution paths [35], and mismatch in the orthogonality of the MIMO channels. These challenges are more severe in the D-band, and must be mitigated through hardware and algorithm techniques.

B. DOA Estimation

The evaluation of two popular DOA estimation algorithms, MUSIC and MVDR, indicates that the MUSIC outperforms the MVDR for large arrays, while the MVDR can provide superior performance for small arrays. In practice, the required computational power, memory, and simulation time are also important criteria in resource-constrained and real-time applications. Furthermore, the emerging deep learning based DOA estimation approaches [36] can provide higher performance and adaptation to operating conditions.

C. Target RCS

In the simulations presented, the target RCS was assumed as $\sigma = 100 \text{ cm}^2$, as an estimate of the human hand RCS for gesture recognition applications [33]. In practice, the target RCS can exhibit significant variations due to the diversity of targets (for example, human hand for gesture sensing or human chest for vital signs monitoring) and their volatile orientation with respect to the radar array. This can result in large changes in the RX SNR [see (15)] and the TX output power requirements. A practical approach is to design the system for a range of target RCS values.

D. Radar Measurement Time

The measurement time, T_{meas} in (15), can be increased to achieve a higher RX SNR and lower the required TX output power (for example, a gain of 10 dB by increasing it from 1 ms to 10 ms). However, this results in a higher power consumption of the radar, more computational resources to process the received signal samples, and longer processing times. Therefore, the measurement time should be selected based on all of these criteria.

E. TX Output Power Requirement

The TX output power is linearly dependent on the RX SNR through (15). The gain of TX and RX antennas as well as NF of the RX are usually limited by the implementation technology. The radar measurement time can be changed within the

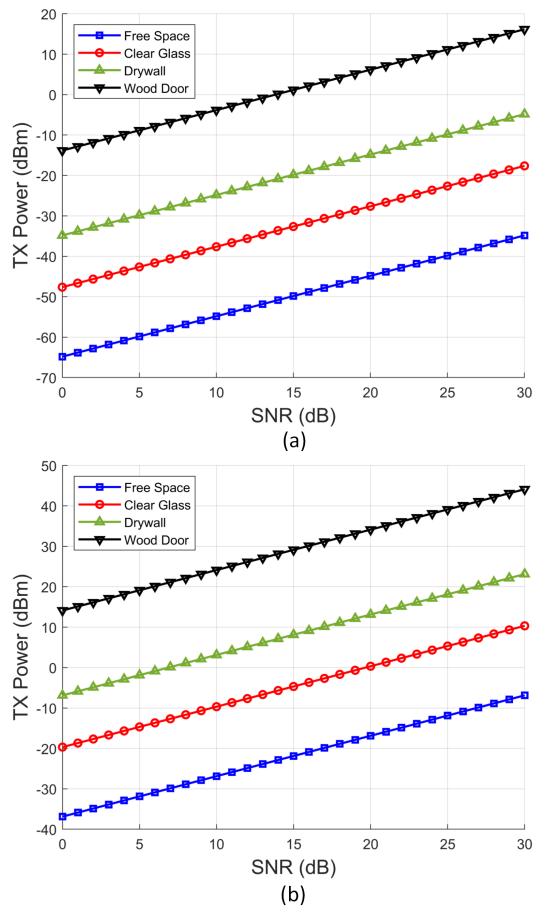


Fig. 14. The required TX output power versus the RX SNR for different indoor materials. (a) 1 m distance, (b) 5 m distance.

practical limits. In the through-wall sensing scenario, a higher TX output power is required to compensate for the extra losses. In practice, there are other losses due to wave scattering by the material in the D-band [2]. Therefore, the radar should be able to provide a wide range of TX output power.

F. Power Consumption

The power consumption of the radar array is dominated by the RX and LO circuits under the condition that a low SNR is sufficient for the DOA estimation. However, in the high-SNR regime, the power consumption is significantly dependent on the SNR. In the large radar arrays implemented on silicon processes, the density of power consumption (per unit area) is very high in the D-band, and should be properly managed through the packaging and heatsink considerations.

VI. CONCLUSION

We presented an algorithm-hardware system design approach of 2D multi-input multi-output (MIMO) frequency-modulated continuous-wave (FMCW) radar arrays for D-band indoor wireless sensing. The directional-of-arrival (DOA) estimation in the presence of noise was evaluated using the MUSIC and MVDR algorithms. It was shown that the MUSIC algorithm can provide higher accuracy and faster simulations

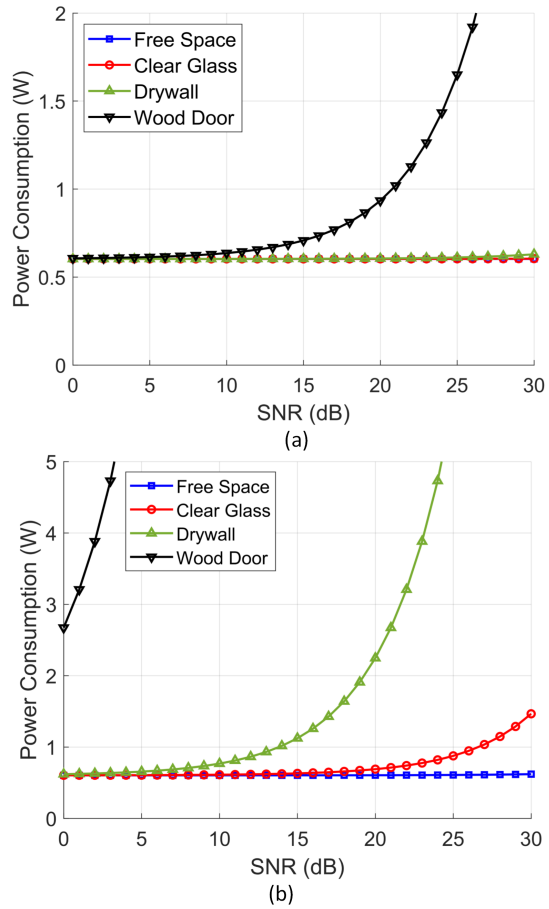


Fig. 15. Power consumption of the radar array with 64 elements versus the RX SNR for different indoor materials. (a) 1 m distance, (b) 5 m distance.

for large arrays, while the MVDR algorithm outperforms for small arrays. A scaling approach was developed for the transmitted output power and received SNR with distance, which could significantly reduce the required output power and power consumption. A hardware model was developed to estimate the power consumption of the radar array. The LO amplifiers are distributed within the LO network to compensate for the passive losses with a fair increase in the power consumption. Performance of the radar array in the free-space and through-wall indoor wireless sensing scenarios was investigated and promising results were achieved for future applications in the D-band.

REFERENCES

- [1] C. de Lima *et al.*, (Eds.). (2020). 6G white paper on localization and sensing. 6G Research Visions, No. 12. University of Oulu. <http://urn.fi/urn:isbn:9789526226743>
- [2] T. S. Rappaport *et al.*, "Wireless communications and applications above 100 GHz: Opportunities and challenges for 6G and beyond," *IEEE Access*, vol. 7, pp. 78729–78757, June 2019, doi: 10.1109/ACCESS.2019.2921522.
- [3] T. Maiwald *et al.*, "A review of integrated systems and components for 6G wireless communication in the D-band," *Proc. IEEE*, vol. 111, no. 3, pp. 220–256, March 2023, doi: 10.1109/JPROC.2023.3240127.
- [4] S. Kim, W. T. Khan, A. Zajic and J. Papapolymou, "D-band channel measurements and characterization for indoor applications," *IEEE Trans. Antennas Propag.*, vol. 63, no. 7, pp. 3198–3207, July 2015, doi: 10.1109/TAP.2015.2426831.

- [5] B. De Beelde, D. Plets, C. Desset, E. Tanghe, A. Bourdoux and W. Joseph, "Material characterization and radio channel modeling at D-band frequencies," *IEEE Access*, vol. 9, pp. 153528–153539, Nov. 2021, doi: 10.1109/ACCESS.2021.3127399.
- [6] A. Visweswaran *et al.*, "A 28-nm-CMOS based 145-GHz FMCW radar: System, circuits, and characterization," *IEEE J. Solid-State Circuits*, vol. 56, no. 7, pp. 1975–1993, July 2021, doi: 10.1109/JSSC.2020.3041153.
- [7] B. Sene, D. Reiter, H. Knapp, H. Li, T. Braun and N. Pohl, "An automotive D-band FMCW radar sensor based on a SiGe-transceiver MMIC," *IEEE Microw. Wireless Compon. Lett.*, vol. 32, no. 3, pp. 194–197, March 2022, doi: 10.1109/LMWC.2021.3121656.
- [8] M. Furqan, F. Ahmed and A. Stelzer, "A D-band fully-integrated 2-RX, 1-TX FMCW radar sensor with 13dBm output power," *Eur. Microwave Integrated Circuits Conf. (EuMIC)*, Paris, France, 2019, pp. 100–103, doi: 10.23919/EuMIC.2019.8909441.
- [9] W. A. Ahmad *et al.*, "Multimode W-band and D-band MIMO scalable radar platform," *IEEE Trans. Microw. Theory Techn.*, vol. 69, no. 1, pp. 1036–1047, Jan. 2021, doi: 10.1109/TMTT.2020.3038532.
- [10] W. Deng *et al.*, "A D-band joint radar-communication CMOS transceiver," *IEEE J. Solid-State Circuits*, vol. 58, no. 2, pp. 411–427, Feb. 2023, doi: 10.1109/JSSC.2022.3185160.
- [11] A. Zandieh, S. Bonen, M. S. Dadash, M. J. Gong, J. Hasch and S. P. Voinescu, "155 GHz FMCW and stepped-frequency carrier OFDM radar sensor transceiver IC featuring a PLL with <30 ns settling time and 40 fs rms jitter," *IEEE Trans. Microw. Theory Techn.*, vol. 69, no. 11, pp. 4908–4924, Nov. 2021, doi: 10.1109/TMTT.2021.3094189.
- [12] H. J. Ng, M. Kucharski, W. Ahmad and D. Kissinger, "Multi-purpose fully differential 61- and 122-GHz radar transceivers for scalable MIMO sensor platforms," *IEEE J. Solid-State Circuits*, vol. 52, no. 9, pp. 2242–2255, Sept. 2017, doi: 10.1109/JSSC.2017.2704602.
- [13] S. Park *et al.*, "A D-band low-power and high-efficiency frequency multiply-by-9 FMCW radar transmitter in 28-nm CMOS," *IEEE J. Solid-State Circuits*, vol. 57, no. 7, pp. 2114–2129, July 2022, doi: 10.1109/JSSC.2022.3157643.
- [14] R. Nikandish, "GaN integrated circuit power amplifiers: Developments and prospects," *IEEE J. Microwaves*, vol. 3, no. 1, pp. 441–452, Jan. 2023, doi: 10.1109/JMW.2022.3221268.
- [15] E. Fishler, A. Haimovich, R. Blum, D. Chizhik, L. Cimini and R. Valenzuela, "MIMO radar: an idea whose time has come," *Proc. IEEE Radar Conf.*, 2004, pp. 71–78, doi: 10.1109/NRC.2004.1316398.
- [16] J. Li and P. Stoica, "MIMO radar with colocated antennas," *IEEE Signal Process. Mag.*, vol. 24, no. 5, pp. 106–114, Sept. 2007, doi: 10.1109/MSP.2007.904812.
- [17] A. Di Serio, P. Hüglér, F. Roos and C. Waldschmidt, "2-D MIMO radar: A method for array performance assessment and design of a planar antenna array," *IEEE Trans. Antennas Propag.*, vol. 68, no. 6, pp. 4604–4616, June 2020, doi: 10.1109/TAP.2020.2972643.
- [18] X. Zhuge and A. G. Yarovoy, "Study on two-dimensional sparse MIMO UWB arrays for high resolution near-field imaging," *IEEE Trans. Antennas Propag.*, vol. 60, no. 9, pp. 4173–4182, Sep. 2012.
- [19] Z. Peng and C. Li, "A portable K-band 3-D MIMO radar with nonuniformly spaced array for short-range localization," *IEEE Trans. Microw. Theory Techn.*, vol. 66, no. 11, pp. 5075–5086, Nov. 2018, doi: 10.1109/TMTT.2018.2869565.
- [20] K. Tan *et al.*, "On sparse MIMO planar array topology optimization for UWB near-field high-resolution imaging," *IEEE Trans. Antennas Propag.*, vol. 65, no. 2, pp. 989–994, Feb. 2017, doi: 10.1109/TAP.2016.2632626.
- [21] A. Puglielli *et al.*, "Design of energy- and cost-efficient massive MIMO arrays," *Proc. IEEE*, vol. 104, no. 3, pp. 586–606, March 2016, doi: 10.1109/JPROC.2015.2492539.
- [22] E. Torkildson, U. Madhow and M. Rodwell, "Indoor millimeter wave MIMO: Feasibility and performance," *IEEE Trans. Wireless Commun.*, vol. 10, no. 12, pp. 4150–4160, December 2011, doi: 10.1109/TWC.2011.092911.101843.
- [23] R. Nikandish, A. Yousefi and E. Mohammadi, "Spurs in millimeter-wave FMCW radar system-on-chip," *IEEE Trans. Radar Syst.*, vol. 1, pp. 21–33, Dec. 2023, doi: 10.1109/TRS.2023.3265845.
- [24] B. T. Arnold and M. A. Jensen, "The effect of antenna mutual coupling on MIMO radar system performance," *IEEE Trans. Antennas Propag.*, vol. 67, no. 3, pp. 1410–1416, March 2019, doi: 10.1109/TAP.2018.2888702.
- [25] R. Schmidt, "Multiple emitter location and signal parameter estimation," *IEEE Trans. Antennas Propag.*, vol. 34, no. 3, pp. 276–280, March 1986, doi: 10.1109/TAP.1986.1143830.
- [26] J. Capon, "High-resolution frequency-wavenumber spectrum analysis," *Proc. IEEE*, 1969, Vol. 57, pp. 1408–1418
- [27] S. Sun, A. P. Petropulu and H. V. Poor, "MIMO radar for advanced driver-assistance systems and autonomous driving: Advantages and challenges," *IEEE Signal Process. Mag.*, vol. 37, no. 4, pp. 98–117, July 2020, doi: 10.1109/MSP.2020.2978507.
- [28] W. L. Stutzman and G. A. Thiele, *Antenna Theory and Design*. Third Ed., John Wiley & Sons, 2012.
- [29] X. Gu, D. Liu and B. Sadhu, "Packaging and antenna integration for silicon-based millimeter-wave phased arrays: 5G and beyond," *IEEE J. Microwaves*, vol. 1, no. 1, pp. 123–134, Jan. 2021, doi: 10.1109/JMW.2020.3032891.
- [30] X. Tang *et al.*, "Design of D-band transformer-based gain-boosting class-AB power amplifiers in silicon technologies," *IEEE Trans. Circuits Syst. I: Reg. Papers*, vol. 67, no. 5, pp. 1447–1458, May 2020, doi: 10.1109/TCSI.2020.2974197.
- [31] H. Khatibi, S. Khyabani, and E. Afshari, "A 173 GHz amplifier with a 18.5 dB power gain in a 130 nm SiGe process: A systematic design of high-gain amplifiers above $f_{max}/2$," *IEEE Trans. Microw. Theory Techn.*, vol. 66, no. 1, pp. 201–214, Jan. 2018, doi: 10.1109/TMTT.2017.2727038.
- [32] D.-W. Park, D. R. Utomo, B. H. Lam, S.-G. Lee, and J.-P. Hong, "A 230–260-GHz wideband and high-gain amplifier in 65-nm CMOS based on dual-peak G_{max} -core," *IEEE J. Solid-State Circuits*, vol. 54, no. 6, pp. 1613–1623, Jun. 2019, doi: 10.1109/JSSC.2019.2899515.
- [33] P. Hüglér, M. Geiger and C. Waldschmidt, "RCS measurements of a human hand for radar-based gesture recognition at E-band," *German Microwave Conference (GeMiC)*, Bochum, Germany, 2016, pp. 259–262, doi: 10.1109/GEMIC.2016.7461605.
- [34] F. Adib and D. Katabi, "See through walls with WiFi!," *SIGCOMM Comput. Commun. Rev.* 43, 4, Oct. 2013, 75–86. <https://doi.org/10.1145/2534169.2486039>
- [35] J. Zhang, A. Singhvi, S. S. Ahmed and A. Arbabian, "18.1 A W-band transceiver array with 2.4 GHz LO synchronization enabling full scalability for FMCW radar," *IEEE Int. Solid-State Circuits Conf. (ISSCC) Dig. Tech. Papers*, San Francisco, CA, USA, 2023, pp. 282–284, doi: 10.1109/ISSCC42615.2023.10067317.
- [36] G. K. Papageorgiou, M. Sellathurai and Y. C. Eldar, "Deep networks for direction-of-arrival estimation in low SNR," *IEEE Trans. Signal Process.*, vol. 69, pp. 3714–3729, 2021, doi: 10.1109/TSP.2021.3089927.